Nanoscale

PAPER

View Article Online
View Journal | View Issue

Check for updates

Cite this: *Nanoscale*, 2024, **16**, 4047

Emerging electrospinning platform toward nanoparticle to single atom transformation for steering selectivity in ammonia synthesis†

Xuan Zheng,[a] Jiace Hao,[a] Zechao Zhuang,[b] Qi Kang,[c] Xiaofan Wang,[a] Shuanglong Lu, [a] Fang Duan, [a] Mingliang Du *[a] and Han Zhu *[a]

The rising top-down synthetic methodologies for transition metal single-atom catalysts (SACs) require controlled movement of metal atoms through the substrates; however, their direct transportation towards the ideal carrier remains a huge challenge. Herein, we showed a "top down" strategy for Co nanoparticles (NPs) to Co SA transformation by employing electrospun carbon nanofibers (CNFs) as atom carriers. Under high-temperature conditions, the Co atoms migrate from the surfaces of Co NPs and are then anchored by the surrounding carbon to form a Co-C_3O_1 coordination structure. The synthesized Co SAs/CNF electrocatalyst exhibits excellent electrocatalytic nitrate reduction reaction (NO_3RR) activity with an NH_3 yield of 0.79 mmol h^{-1} cm^{-2} and Faraday efficiency (FE) of 91.3% at −0.7 V *vs.* RHE in 0.1 M KNO_3 and 0.1 M K_2SO_4 electrolytes. The *in situ* electrochemical characterization suggests that the NOH pathway is preferred by Co SAs/CNFs, and *NO hydrogenation and deoxygenation easily occur on Co SAs due to the small adsorption energy between Co SAs and *NO, as calculated by theoretical calculations. It is revealed that a small energy barrier (0.45 eV) for the rate determining step (RDS) ranges from *NO to *NOH and a strong capability for inhibiting hydrogen evolution (HER) significantly promotes the NH_3 selectivity and activity of Co SAs/CNFs.

Received 22nd October 2023,
Accepted 30th January 2024

DOI: 10.1039/d3nr05331h

rsc.li/nanoscale

Published on 31 January 2024. Downloaded on 12/2/2024 2:15:32 PM.

Introduction

Ammonia is well known as a ubiquitous industrial raw material and efficient energy carrier with elevated hydrogen density.[1,2] The traditional ammonia synthesis through the Haber–Bosch process depends on the reaction of N_2 and H_2 that requires vast amounts of energy consumption (450 °C, 200 bar), resulting in staggering carbon emissions. Consequently, there has been growing interest in ammonia synthesis by applying electrochemical techniques under mild conditions, such as electrochemical nitrogen reduction reaction (NRR) and nitrate reduction reaction (NO_3RR).[3–6] The NRR process usually suffers from low faradaic efficiency (FE) and NH_3 yield rate owing to the ultra-stable N≡N triple bond (941 kJ mol^{-1}). Meanwhile, compared with NRR, NO_3RR has emerged as a promising alternative for electrochemical NH_3 production owing to the excellent water solubility of NO_3^- and the low dissociation energy of N=O bonds (204 kJ mol^{-1}).[7–9] The NO_3RR process involves an eight-electron transfer reaction, which is commonly impeded by competitive hydrogen evolution reaction (HER) and NO_2^- production. Therefore, the development of advanced electrocatalysts for NO_3RR with high selectivity and durability is highly desirable.

In recent years, single-atom catalysts (SACs) have attracted widespread attention in the electrocatalysis field owing to their excellent catalytic activities.[10–12] "Top down" and "bottom up" are two general strategies for the synthesis of SACs. In "bottom up" strategies, metal–organic frameworks (MOFs) are the widely used substrates for anchoring the SA under high temperatures.[13,14] However, owing to their high surface energy and low coordination numbers, the synthesis of stable SA still suffers from the aggregation trend into larger nanoparticles (NPs) during the following thermal process at high temperatures, which may reduce their catalytic performance.[15–17] For the "top down" strategies, the MOF-derived carbon has limited vacant sites for metal atom confinement, which leads to a mixed existence of SA and NP and small metal loading of SA.[15] Accordingly, developing novel strategies to overcome these limitations in the synthesis of SACs is highly desirable. However, controlling the movement of metal atoms through

[a]*Key Laboratory of Synthetic and Biological Colloids, Ministry of Education, School of Chemical and Material Engineering, Jiangnan University, Wuxi 214122, China. E-mail: zhysw@jiangnan.edu.cn, du@jiangnan.edu.cn*
[b]*Department of Chemical Engineering, Columbia University, New York, NY, 10027, USA*
[c]*Institute of New Energy for Vehicles, School of Materials Science and Engineering, Tongji University, Shanghai, 201804, China*
† Electronic supplementary information (ESI) available. See DOI: https://doi.org/10.1039/d3nr05331h

Published on 31 January 2024. Downloaded on 12/2/2024 2:15:32 PM.

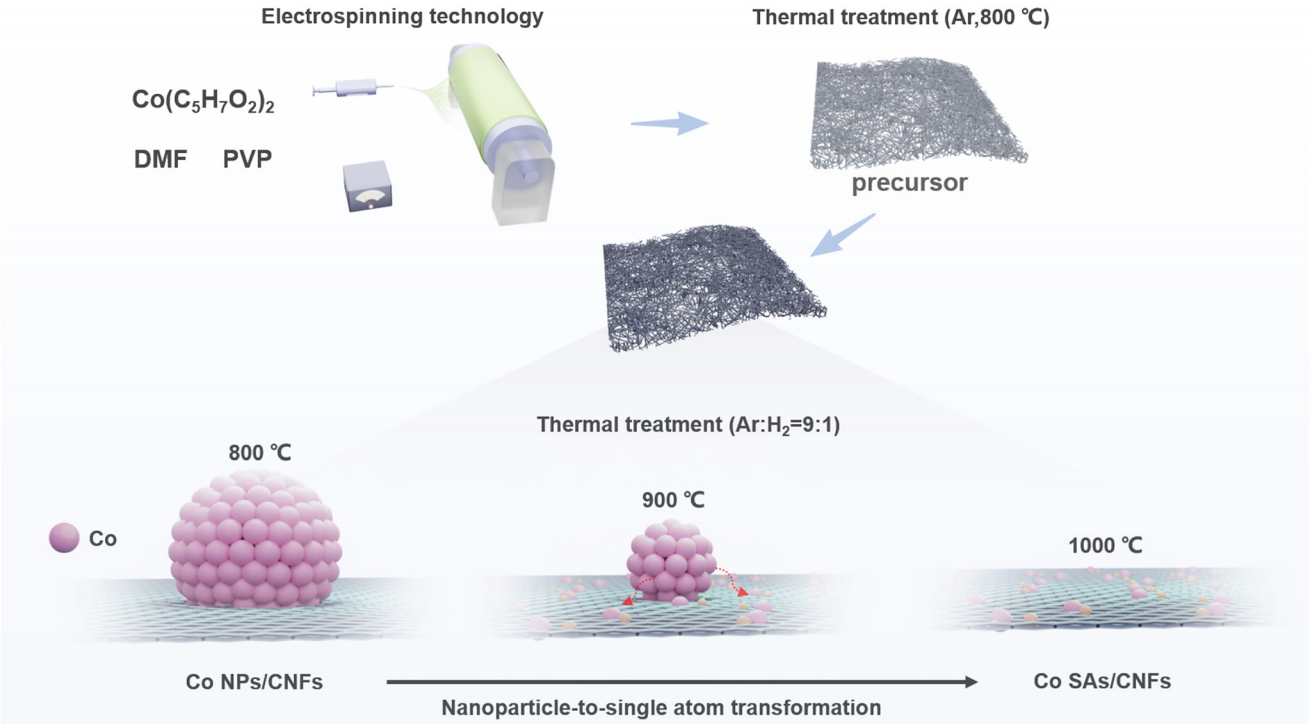

Scheme 1 Schematic illustration of the preparation process of Co SAs/CNFs.

the substrates and directly transporting them towards the ideal carrier remain huge challenges in the field of SAC preparation.

Herein, we used electrospun nanofiber as an atom carrier to control the transformation from Co NPs to Co SAs. Under high-temperature treatment, the Co atoms migrate from the surfaces of preformed Co NPs in carbon nanofibers (Co NPs/CNFs), and the Co atoms are further coordinated by the surrounding carbon to form a Co-C_3O_1 coordination structure, suggesting controlled NP-to-SA transformation. The synthesized Co SA/CNF electrocatalyst exhibits excellent NO_3RR activity with an NH_3 yield of 0.79 mmol h^{-1} cm^{-2} and an FE of 91.3% at −0.7 V *vs.* RHE in 0.1 M KNO_3 and 0.1 M K_2SO_4 electrolytes, respectively. *In situ* electrochemical characterization verified the formation of critical reaction intermediates during the reaction, that is, Co SAs/CNFs preferred to react in the reaction pathway of $*NO_3^- \rightarrow *NO_2^- \rightarrow *NO \rightarrow *NOH \rightarrow *N \rightarrow *NH \rightarrow *NH_2 \rightarrow *NH_3$. Theoretical calculations reveal that Co SAs show a smaller energy barrier for the RDS step of *NO to *NOH when compared with Co NPs, leading to superior selectivity in ammonia synthesis.

Han Zhu

Han Zhu received his Ph.D. degree from Zhejiang Sci-Tech University in 2016 under the supervision of Prof. Mingliang Du. In 2017, he joined the School of Chemical and Materials Engineering at Jiangnan University as an Associate Professor. His current research interests mainly focus on the design and synthesis of electrospun nanofiber-based novel nanostructured materials applied in electrocatalysis, heterogeneous catalysis, electrochemical sensors and environmental catalysis.

Results and discussion

The synthesis procedure for the nanoparticle-to-single-atom (NP-to-SA) is illustrated in Scheme 1. Initially, the cobalt acetylacetonate was dissolved in a mixed solution containing PVP and *N*,*N*-Dimethylformamide (DMF), and then the homogeneous solution was electrospun into $Co(C_5H_7O_2)_2$/PVP nanofibers. This transformation process from Co NPs to Co SAs supported on PVP-derived carbon nanofibers (CNFs) was controlled by regulating thermal treatment conditions.

As depicted in Fig. 1a and S1,† densely and uniformly Co NPs with sizes ranging from 7.48 ± 4.5 nm were *in situ* synthesized in CNFs at 800 °C under Ar atmosphere. The Co NPs were completely encapsulated in graphitized carbon shells *via* the self-catalyzed conversion of amorphous carbon by the Co NPs (Fig. 1b). The interplanar spacing of 0.18 nm corresponds to the (200) planes of the Co NPs. Scanning transmission elec-

 This journal is © The Royal Society of Chemistry 2024

Published on 31 January 2024. Downloaded on 12/2/2024 2:15:32 PM.

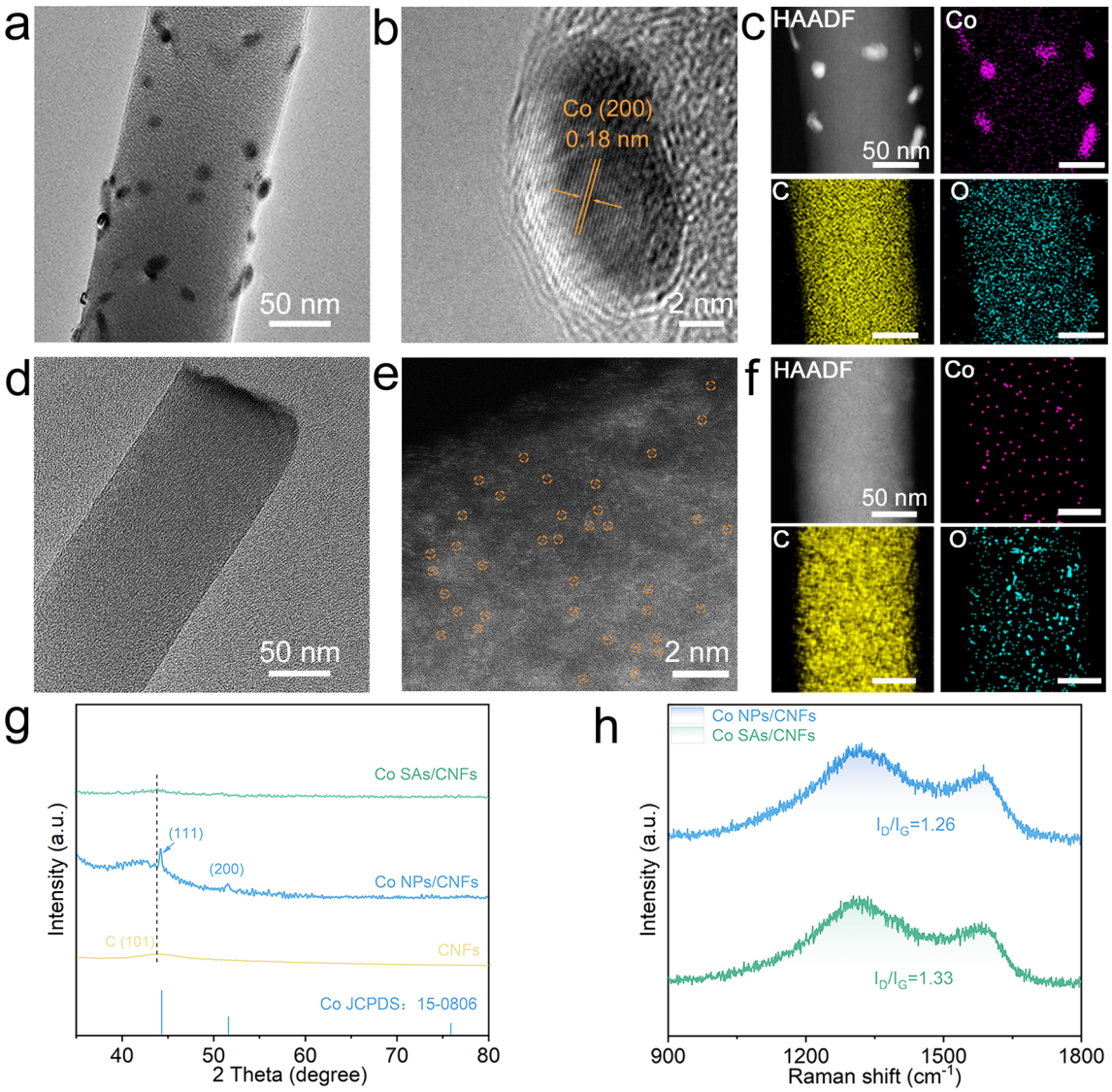

Fig. 1 (a) TEM, (b) HRTEM and (c) STEM-EDS mapping images of Co NPs/CNFs. (d) TEM, (e) aberration-corrected HAADF-STEM and (f) STEM-EDS mapping images of Co SAs/CNFs. (g) XRD patterns of Co SAs/CNFs, Co NPs/CNFs, and CNFs. (h) Raman spectra of Co SAs/CNFs and Co NPs/CNFs.

tron microscopy energy-dispersive spectroscopy (STEM-EDS) mapping images of Co NPs/CNFs show a uniform distribution of C and O elements, which can be attributed to the PVP-derived CNFs (Fig. 1c). The Co element distribution was according to the Co NP morphology, which can also be verified by the corresponding line scan EDS spectra (Fig. S2†). The initial near-spherical Co NPs turned to irregularity with decreased size (3–5 nm) when the Co NPs/CNFs were heated to 900 °C.

Meanwhile, the atomically dispersed Co atoms emerged around the Co NPs, suggesting the cleavage of Co–Co bonds from the Co NPs triggered by the elevated temperature, as revealed by the HAADF-STEM image (Fig. S3†) and STEM-EDS mapping images (Fig. S4†) of Co NPs-Co SAs/CNFs (900 °C). Atomical-resolution high-angle annular dark-field STEM image (Fig. 1d and e) indicates that the Co NPs completely vanished when the Co NPs/CNFs were further heated to 1000 °C. Abundant atomically dispersed Co atoms identified as bright spots were observed on the CNF substrates. Meanwhile, Fig. S5† illustrates the disappearance of Co NPs, suggesting the successful transformation from Co NPs to Co SAs. STEM-EDS mapping images confirm the homogeneous distribution of Co across the entire CNFs without any aggregation of Co elements (Fig. 1f). Inductively coupled plasma-atomic emission spectrometry (ICP-AES) shows that the Co content in Co SAs/CNFs was 0.37 wt%, which was similar to that of Co NPs/CNFs (0.32 wt%, Table S1†). The atomical transformation from Co NPs to Co SAs was further investigated using X-ray diffraction (XRD). As shown in Fig. 1g, the broad bands located at 44.0° correspond to the (101) planes of graphite carbon,[18] which were observed in CNFs, Co NP/CNFs and Co SA/CNFs. The Co NPs/CNFs show typical diffraction peaks assigned to

Published on 31 January 2024. Downloaded on 12/2/2024 2:15:32 PM.

the (111) and (200) planes of the face-centered cubic (fcc) cobalt phase. However, no characteristic peak was detected for the Co crystals in the Co SA/CNFs, which is consistent with the STEM results. Raman spectra (Fig. 1h) further confirmed the relatively higher degree of defected carbon structures in Co SAs/CNFs with a higher I_D/I_G value (1.33),[19] which is beneficial for the trapping and anchoring of Co SAs.

The chemical states and coordination environments of Co SAs/CNFs were investigated using X-ray absorption spectroscopy (XAS). As shown in Fig. 2a, the Co K-edge X-ray absorption near-edge structure (XANES) of Co SAs/CNFs shows a white line peak between the Co foil and CoO, indicating that the Co SAs carry a positive charge and show the 0 to +2 oxidation state of Co. The corresponding Fourier-transformed (FT) k^3-weighted extended X-ray absorption fine structure (EXAFS) spectra (Fig. 2b) suggested that no Co–Co bonds were observed in the Co SAs/CNFs, suggesting that the Co NPs were completely transformed into Co SAs in the CNF matrix. This suggested that there were no Co NPs or clusters in Co SAs/CNF, which were consistent with the STEM and XRD results. The broad and asymmetric peaks located at ~1.8 Å were ascribed to the Co–C or Co–O coordination. X-ray photoelectron spectroscopy (XPS) of Co SAs/CNFs and Co NPs/CNFs is shown in Fig. 2c and Fig. S6, S7.† The binding energies (BEs) for Co–O and Co–C bonds in Co SAs/CNFs emerged at 780.0 eV and 782.5 eV, respectively, suggesting the coordination of Co with C and O.[20–22] The binding energies at 778.6 eV and 793.6 eV observed in the Co 2p XPS spectra provided evidence for the presence of metallic cobalt (Co^0) in the Co NPs/CNFs, while these characteristic peaks were absent in the Co SAs/CNFs, which are consistent with our previous findings from XRD and TEM results. The high-resolution O 1s XPS spectra (Fig. S7†) of Co SAs/CNFs and Co NPs/CNFs both show two peaks attributed to Co–O and C–O bonds, again proving the existence of coordination.[22,23]

Quantitative analysis of EXAFs at the Co K-edge was performed by fitting theoretical EXAF spectra to experimental data in R-space and K-space (Fig. S8†) to further understand the Co coordination environment. It was observed that the fitting curves matched quite well with the experimental spectra. Each Co central atom in the first shell has a coordination number of four and is directly connected by three C atoms and one O atom, with average bond lengths of 2.07 Å and 1.96 Å, respectively (Table S2†). Meanwhile, owing to the powerful resolution in both K and R spaces, the Co K edge wavelet transform (WT)-EXAFS was applied to investigate the atomic configuration of the Co SAs/CNFs. The wavelet transform (WT) plots of Co SA/CNFs further reveal the maximum peak at 6.0 $Å^{-1}$ attributed to the Co–C_3O_1 bonds (Fig. 2d–f).

The electrocatalytic NO_3RR performance of Co NPs/CNFs and Co SAs/CNFs was investigated in H-type cells with Ar-saturated aqueous electrolyte containing 0.5 M K_2SO_4 and 0.1 M

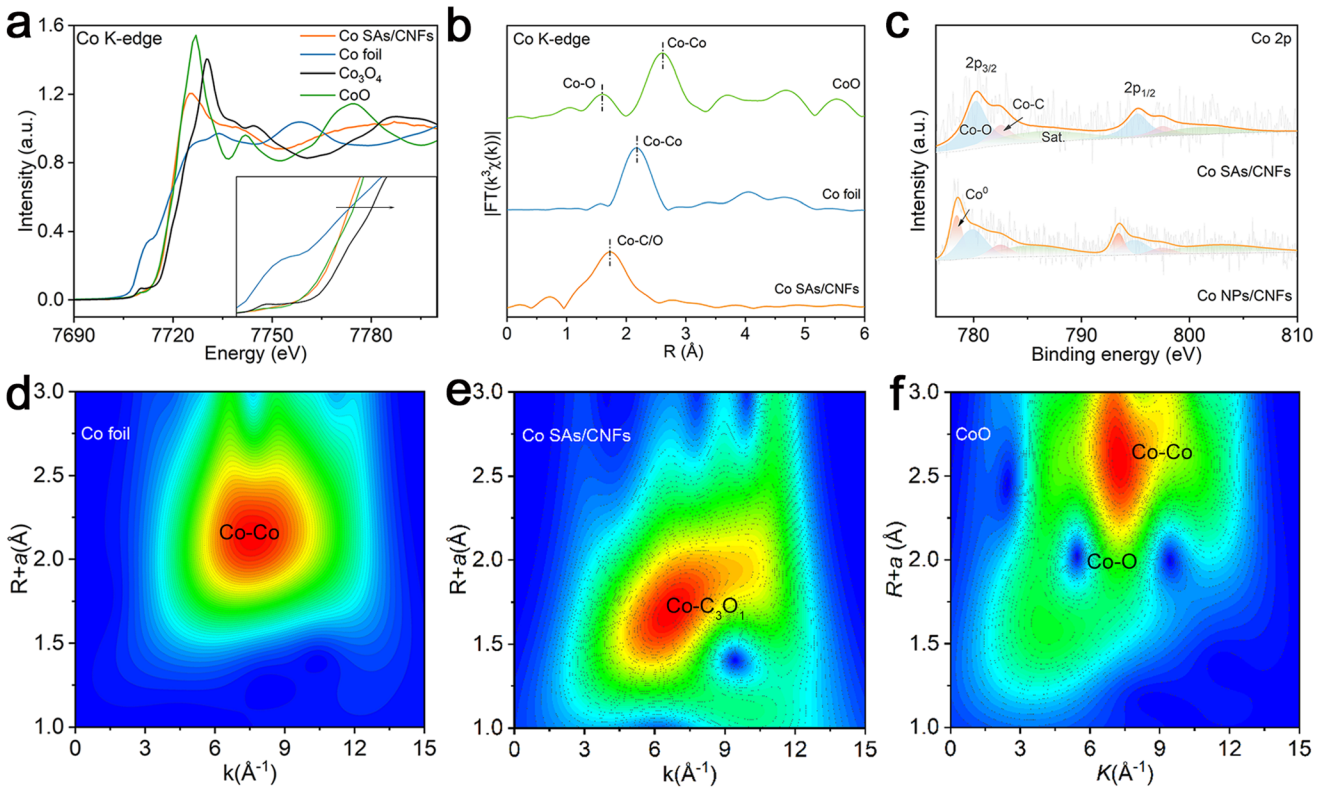

Fig. 2 (a) Co K-edge XANES and (b) Co K-edge EXAFS spectra for Co SAs/CNFs, as well as the reference samples (Co foil, Co_3O_4, and CoO). (c) Co 2p XPS spectra of the Co SAs/CNFs and Co NPs/CNFs. (d–f) WT-EXAFS contour plots of Co foil, Co SAs/CNFs, and CoO foil.

This journal is © The Royal Society of Chemistry 2024

Published on 31 January 2024. Downloaded on 12/2/2024 2:15:32 PM.

KNO_3 (Fig. S9†). Fig. S10† shows the linear sweep voltammetry (LSV) curves of the Co SAs/CNFs, indicating higher current density in the presence of NO_3^- from 0 to −1.10 V *vs.* RHE than that without NO_3^- conditions, suggesting the participation of NO_3^- in the NO_3RR process. As shown in Fig. 3a, the current density of Co SAs/CNFs can reach −74 mA cm^{-2} at −0.7 V *vs.* RHE, which is significantly higher than that of Co NPs/CNFs (−32 mA cm^{-2}), indicating that Co SAs/CNFs could significantly enhance the NO_3RR activity. The chronoamperometry curves of Co SAs/CNFs, Co NPs/CNFs and pure CNFs were measured at various potentials (−0.4 ~ −0.8 V *vs.* RHE) to quantify the NO_3RR performance with FEs and yields of different products, including nitrite (NO_2^-), H_2 and NH_3 (Fig. S11–S13†). The liquid products (NH_4^+, NO_2^- and N_2H_4) were detected by ultraviolet–visible spectroscopy (UV-Vis) (Fig. S14–S16†), while the gas product (H_2) was detected by online gas chromatography (GC). As expected, the Co SAs/CNFs show the NH_4^+ FE (FE_{NH4+}) of 91.3% at −0.7 V *vs.* RHE, which is higher than that of Co NPs/CNFs (FE_{NH4+} of 61.5%) and pure CNFs (FE_{NH4+} of 27.5%) at −0.7 V *vs.* RHE (Fig. 3b and S17†). Both of the FE_{NH4+} and NH_4^+ yield rates (Y_{NH4+}) for Co SAs/CNFs exhibit volcano curves ranging from −0.4 to −0.8 V *vs.* RHE. The Co SAs/CNFs display the Y_{NH4+} of 0.79 mmol h^{-1} cm^{-2} at −0.7 V *vs.* RHE, which is 2.5 times higher than those of Co NPs/CNFs (Y_{NH4+} = 0.31 μmol h^{-1} cm^{-2}) at 0.5 V *vs* RHE, suggesting the key role of Co SAs in the NO_3RR (Fig. 3c). In addition, the possible N_2H_4 byproducts were not detected in the electrolyte after testing (Fig. S11–

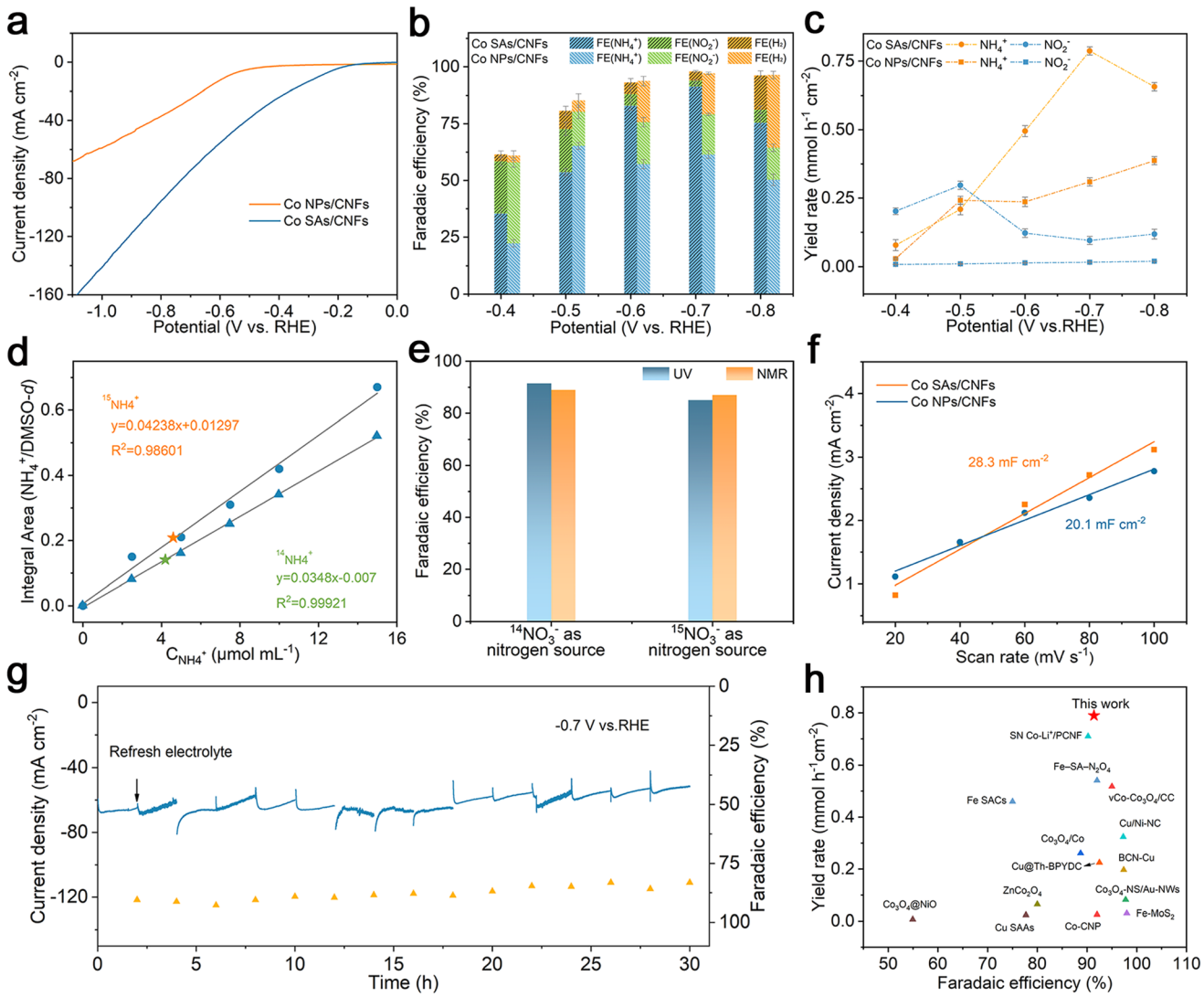

Fig. 3 (a) LSV curves of Co SAs/CNFs and Co NPs/CNFs recorded in 0.5 M K_2SO_4 with and without 0.1 M KNO_3. (b) FEs of different products (NH_4^+, NO_2^- and H_2) at various potentials for Co SAs/CNFs and Co NPs/CNFs. (c) Yield rates of different products (NH_4^+ and NO_2^-) at various potentials for Co SAs/CNFs and Co NPs/CNFs. (d) Calibration curves of peak area between $^{14}NH_4^+$/$^{15}NH_4^+$ and DMSO against the concentration of NH_4^+–N. (e) FE of Co SAs/CNFs at −0.7 V *vs.* RHE with $^{15}NO_3^-$ and $^{14}NO_3^-$ as nitrogen sources, detected by UV/Vis and ^1H NMR spectroscopy. (f) Cdl values of the Co SAs/CNFs and Co NPs/CNFs. (g) Stability test (repeated fifteen cycles) and corresponding FE_{NH4+} (yellow triangle) of Co SAs/CNFs. (h) Comparison of Co SAs/CNFs with reported NO_3RR catalyst Y_{NH4+} and FE_{NH4+}.

Published on 31 January 2024. Downloaded on 12/2/2024 2:15:32 PM.

S13†). To confirm the ammonia product that comes from NO_3RR catalyzed by Co SAs/CNFs, several tests are performed to eliminate the disturbance of environmental contamination. We further used ethylene diamine tetraacetic acid (EDTA) as a chelating agent to reveal the origin of NO_3RR activity. As shown in Fig. S18,† when EDTA was added into the electrolyte during the *i–t* curves, the current density decreased immediately, indicating that the Co SAs were the real active sites for NO_3RR.

The isotope labeling was used to trace the N source in NH_3 production. The $^{14}NO_3^-$ and $^{15}NO_3^-$ were used as the feeding nitrogen sources, and the NH_3 products were determined by ^1H nuclear magnetic resonance (NMR) measurements. As shown in Fig. S19,† the doublet peaks of $^{15}NH_4^+$ were observed when $^{15}NO_3^-$ was used as a source, while the detected triplet peaks of $^{14}NH_4^+$ were ascribed to the $^{14}NO_3^-$ source. Fig. 3d depicts that the peak area of ^1H NMR is directly proportional to the NH_3 content using $^{14}NO_3^-$ and $^{15}NO_3^-$ as the feeding nitrogen sources. The FE_{NH4^+} and Y_{NH4^+} calculated by ^1H NMR using $^{14}NO_3^-$ and $^{15}NO_3^-$ as sources agreed with those determined by UV-vis spectroscopy (Fig. 3e). The results demonstrate that the NH_3 products are produced by the NO_3RR. The electrochemical impedance spectroscopy of Co SAs/CNFs (Fig. S20 and Table S3†) exhibits the smallest charge transfer impendence of ~18 Ω when compared with those of the Co NPs/CNFs (~27 Ω), and CNFs (~37 Ω), suggesting the fastest NO_3RR kinetics of Co SAs/CNFs. In addition, the double-layer capacity (C_{dl}) of Co SAs/CNFs is 28.3 mF cm^{-2}, which is significantly higher than that of Co NPs/CNFs (20.1 mF cm^{-2}), which can provide a larger electrochemical active surface area (ECSA) and thus promote the synthesis of ammonia (Fig. 3f and S21†). Interestingly, the LSV curves normalized by ECSA display that the Co SAs/CNFs still exhibit a higher current density when compared with Co NPs/CNFs, demonstrating the intrinsic activity of Co SAs/CNFs (Fig. S22†). In addition, the stability of electrocatalysts is critical in industrial applications. The NO_3RR on Co SAs/CNFs performed at −0.7 V *vs.* RHE for 15 consecutive cycles indicated no significant attenuation, and the FE_{NH4^+} was also maintained around 90%, thus confirming its excellent stability (Fig. 3g). The atomic-scale HAADF-STEM images (Fig. S23†) of Co SAs/CNFs further confirm that the monoatomic morphology of Co is well maintained after long-term NO_3RR electrocatalytic experiments, demonstrating that the stability of coordinated Co-C_3O_1 favors efficient NO_3^- electrolysis into NH_4^+. Furthermore, the CV stability (Fig. S24†) test shows that the current density barely changes after the long-term stability test, which further demonstrates the excellent long-term stability of Co SAs. Finally, the electrocatalytic NO_3RR capability of Co SAs/CNFs was compared with other reported cobalt-containing catalysts or single-atom catalysis. As shown in Fig. 3h and ESI Table S4,† the Co SAs/CNFs demonstrate superior NO_3RR performance in terms of the Y_{NH4^+} and FE_{NH4^+} compared with the recently reported Co-based electrocatalyst.[24–37]

In situ characterization was further used to investigate the reaction pathways over Co SAs/CNFs by directly identifying the reaction intermediates. The identification of potential intermediates generated during the NO_3RR was explored by online differential electrochemical mass spectrometry (DEMS, Fig. 4a). The DEMS signals recorded at −0.7 V *vs.* RHE show that m/z = 31, 30, 17, 16, 15, and 14, which were ascribed to the NOH, NO, NH_3, NH_2, NH, and N intermediates, respectively. Notably, the key intermediate of $*NH_2OH$ for the NHO pathway was not detected. This observation suggests that the NOH pathway is the main pathway preferred by Co SAs/CNFs, which involves the following steps: $*NO \rightarrow *NOH \rightarrow *N \rightarrow *NH \rightarrow *NH_2 \rightarrow *NH_3$. *In situ* Raman spectroscopy recorded on Co SAs/CNFs during the NO_3RR electrolysis is shown in Fig. 4b† and S25.† The peak that emerged at 1080 cm^{-1} was attributed to the absorbed NO_3^- on Co SAs/CNFs and with a more negative potential ranging from 0 to −1.1 V *vs.* RHE; the peak intensity for NO_3^- continuously decreased, suggesting the NO_3^- consumption for NO_3RR over Co SAs/CNFs.[38,40] In addition, the Raman peak at 982 cm^{-1} was identified as an adsorbed sulfate species (SO_4^{2-}) on the catalyst surface. The above results demonstrate the NO_3RR reaction pathways on Co SAs/CNFs.[39,40]

Density functional theory (DFT) calculations were further used to explore the mechanism of Co SAs. The STEM and EXAFS results were used to construct the Co SAs/CNFs model, and details can be found in the ESI.† According to the HRTEM analysis, the (200) crystal plane is the main exposed facet in the Co NPs; therefore, the Co (100) surface was used as the model for the calculations. Based on the detected intermediates, the reaction pathway was simulated *via* DFT calculations, as presented in Fig. S26† and Fig. 4c. First, the NO_3^- ions were adsorbed on catalyst surfaces to form $*NO_3$, and the decreased total energy indicated a spontaneous reaction. Then, the N–O bond is continuously cleaved through proton-coupled electron transfer to form $*NO_2$ and *NO. Subsequently, under hydrogenation conditions, the *NO intermediate is gradually transformed into *HOH, *N, *NH, and $*NH_2$ and is finally converted to $*NH_3$. The hydrogenation from *NO to *NOH over Co SAs and Co NPs is the rate-determining step (RDS). The Co SAs exhibit Gibbs free energy (ΔG) for an RDS step of 0.45 eV, which is smaller than that of Co NPs (ΔG = 0.78 eV), highlighting the critical role of Co SAs in facilitating the kinetics of NO_3RR. The results demonstrate the superior NO_3RR activity of Co SAs compared to Co NPs. As shown in Fig. 4d, the charge transfer between Co NPs and *NO was 0.49 eV, which was higher than that between Co SAs and *NO (0.25 eV). This indicates that the excessive charge transfer results in a strong adsorption energy between Co NPs and *NO, which could affect *NO hydrogenation and subsequent deoxygenation. Therefore, the *NO hydrogenation and deoxygenation easily occurred on Co SAs. In addition, the density of states (DOS) in relation to the electronic structure and the corresponding d-band center of Co SAs/CNFs (−0.8 eV) and Co NPs/CNFs (−1.4 eV) were also calculated. The lower d-band center for Co SAs/CNFs demonstrates that the distribution of d-band electrons is closer to the Fermi level, resulting in strong absorption for key intermediates of *NOH (Fig. S27†). In addition, the energy barrier for the generation of byproduct H_2 by Co SAs/

 This journal is © The Royal Society of Chemistry 2024

Published on 31 January 2024. Downloaded on 12/2/2024 2:15:32 PM.

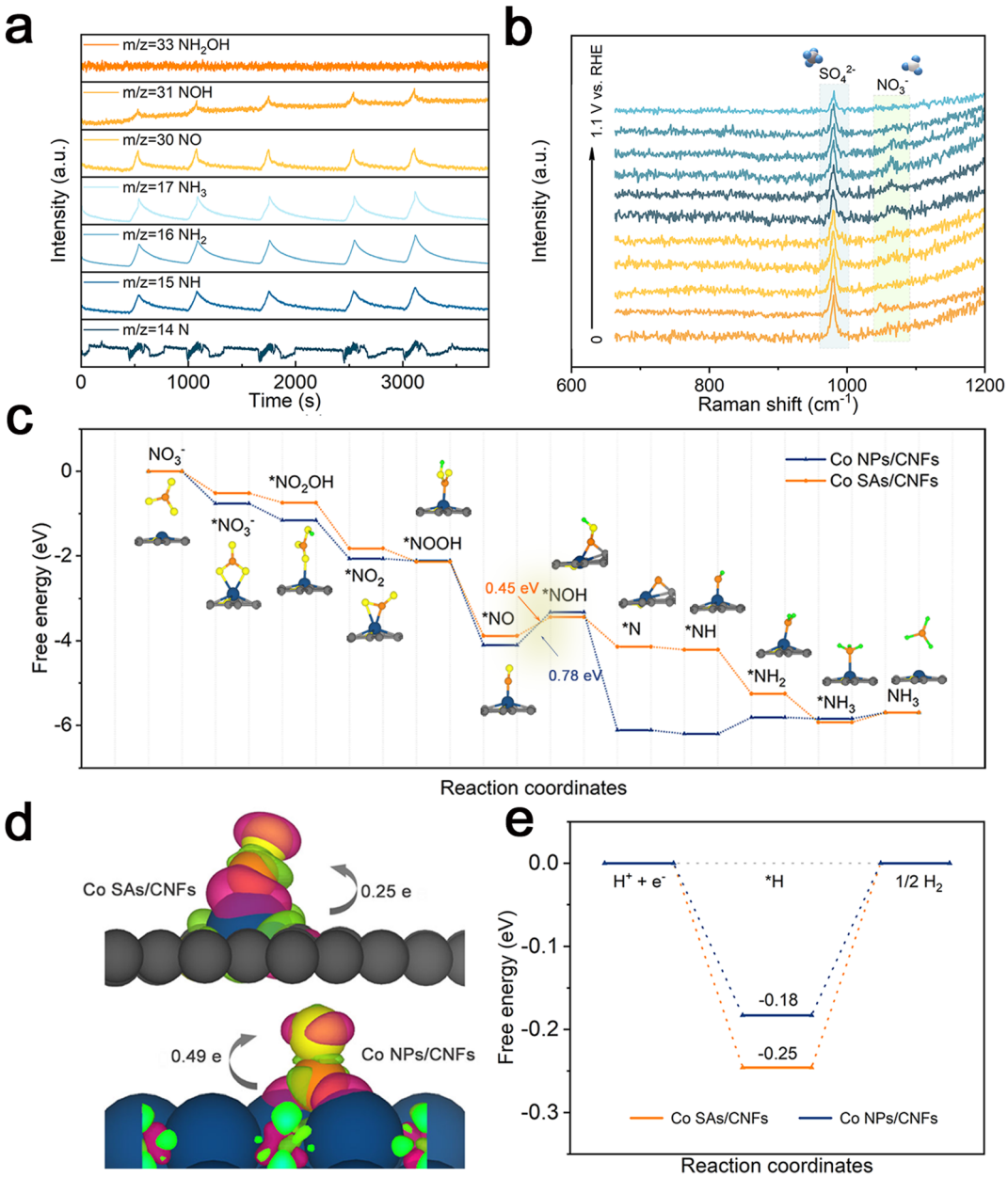

Fig. 4 (a) Online DEMS spectra of Co SAs/CNFs during the NO_3RR electrolysis at −0.7 V *vs.* RHE. (b) *In situ* Raman spectra of Co SAs/CNFs obtained at the potential ranging from 0 to −1.1 V *vs.* RHE. (c) Calculated free energy of NO_3RR pathways on Co SAs/CNFs and Co NPs/CNFs. (d) Bader charge analysis of *NO intermediate formed on Co SAs/CNFs and Co NPs/CNFs. (e) Free energies of H adsorption on Co SAs/CNFs and Co SAs/CNFs.

CNFs is 0.25 eV, which is significantly higher than that of Co NPs/CNFs (0.18 eV), indicating an inhibitory effect of Co SAs/CNFs on H_2 generation (Fig. 4e). The results demonstrate that the Co SAs could significantly reduce the energy barrier of the RDS steps (*NO → *NOH) and suppress the competing HER, thus leading to remarkable electrocatalytic activity.

Conclusion

In summary, we demonstrated a dynamic transformation from Co NPs to Co SAs by combining electrospinning and high-temperature pyrolysis migration strategies. At −0.7 V *vs.* RHE, the FE_{NH4^+} of 91.30% and Y_{NH4^+} of 0.79 μmol h^{-1} cm^{-2} were obtained for Co SAs/CNFs, which were significantly higher than those for Co NPs/CNFs (FE_{NH4^+}, 61.48%; Y_{NH4^+}, 0.31 μmol h^{-1} cm^{-2}). This observation suggests that the NOH pathway is the main pathway preferred by Co SAs/CNFs. The *NO hydrogenation and deoxygenation easily occur on Co SAs owing to the small adsorption energy between Co SAs and *NO, as calculated by DFT. It is found that a small energy barrier (0.45 eV) for the RDS step from *NO to *NOH and a strong capability for inhibiting HER significantly promote the NH_3 selectivity and activity of Co SAs/CNF.

Published on 31 January 2024. Downloaded on 12/2/2024 2:15:32 PM.

Conflicts of interest

The authors declare no conflict of interest.

Acknowledgements

This study was supported by the National Natural Science Foundation of China (NSFC) (52273058, 52073124), Natural Science Foundation of Jiangsu Province (SBK2022030167), Fundamental Research Funds for the Central Universities, and Postgraduate Research & Practice Innovation Program of Jiangsu Province (KYCX23_2467). The authors would also like to thank the characterizations supported by Central Laboratory, School of Chemical and Material Engineering, Jiangnan University.

References

1 D. Liu, L. L. Qiao, S. Y. Peng, H. Y. Bai, C. F. Liu, W. F. Ip, K. H. Lo, H. C. Liu, K. W. Ng, S. P. Wang, X. Z. Yang and H. Pan, Recent Advances in Electrocatalysts for Efficient Nitrate Reduction to Ammonia, *Adv. Funct. Mater.*, 2023, **33**, 2303480.

2 X. X. Yang, S. Y. Mukherjee, T. O'Carroll, Y. Hou, M. R. Singh, J. A. Gauthier and G. Wu, Achievements, Challenges, and Perspectives on Nitrogen Electrochemistry for Carbon-Neutral Energy Technologies, *Angew. Chem.*, 2023, **135**, e202215938.

3 E. Murphy, Y. Liu, I. Matanovic, *et al.*, Elucidating electrochemical nitrate and nitrite reduction over atomically-dispersed transition metal sites, *Nat. Commun.*, 2023, **14**, 4554.

4 P. H. van Langevelde, I. Katsounaros and M. T. M. Koper, Electrocatalytic nitrate reduction for sustainable ammonia production, *Joule*, 2021, **5**, 290–294.

5 Q. L. Hong, B. Q. Miao, T. J. Wang, F. M. Li and Y. Chen, Intermetallic PtTe metallene for formic acid oxidation assisted electrocatalytic nitrate reduction, *Energy Lab.*, 2023, **1**(2), 220022.

6 Z. X. Ge, T. J. Wang, Y. Ding, S. B. Yin, F. M. Li, P. Chen and Y. Chen, Interfacial Engineering Enhances the Electroactivity of Frame-Like Concave RhCu Bimetallic Nanocubes for Nitrate Reduction, *Adv. Energy Mater.*, 2022, **12**, 2103916.

7 Y. T. Wang, C. H. Wang, M. Y. Li, Y. F. Yu and B. Zhang, Nitrate electroreduction: mechanism insight, in situ characterization, performance evaluation, and challenges, *Chem. Soc. Rev.*, 2021, **50**, 6720–6733.

8 I. Muzammil, Y. N. Kim, H. Kang, D. K. Dinh, S. Choi, C. Jung, Y. H. Song, E. Kim, J. M. Kim and D. H. Lee, Plasma catalyst-integrated system for ammonia production from H_2O and N_2 at atmospheric pressure, *ACS Energy Lett.*, 2021, **6**, 3004–3010.

9 H. N. Li, H. Zhu, Z. C. Zhuang, S. L. Lu, F. Duan and M. L. Du, Single-atom catalysts for electrochemical clean energy conversion: recent progress and perspectives, *Sustainable Energy Fuels*, 2020, **4**, 996–1011.

10 W. Song, C. Xiao, J. Ding, Z. Huang, X. Yang, T. Zhang, D. Mitlin and W. Hu, Review of Carbon Support Coordination Environments for Single Metal Atom Electrocatalysts (SACS), *Adv. Mater.*, 2024, **36**, 2301477.

11 L. H. Xu, W. Liu and K. Liu, Single Atom Environmental Catalysis: Influence of Supports and Coordination Environments, *Adv. Funct. Mater.*, 2023, **33**, 2304468.

12 T. Y. Xiang, Y. T. Liang, Y. X. Zeng, J. Deng, J. L. Yuan, W. P. Xiong, B. Song, C. Y. Zhou and Y. Yang, Transition Metal Single-Atom Catalysts for the Electrocatalytic Nitrate Reduction: Mechanism, Synthesis, Characterization, Application, and Prospects, *Small*, 2023, **19**, 2303732.

13 X. Liang, N. H. Fu, S. C. Yao, Z. Li and Y. D. Li, The Progress and Outlook of Metal Single-Atom-Site Catalysis, *J. Am. Chem. Soc.*, 2022, **144**(40), 18155–18174.

14 Z. Li, S. F. Ji, Y. W. Liu, X. Cao, S. B. Tian, Y. J. Chen, Z. Q. Ni and Y. D. Li, Well-Defined Materials for Heterogeneous Catalysis: From Nanoparticles to Isolated Single-Atom Sites, *Chem. Rev.*, 2020, **120**(2), 623–682.

15 J. Yang, Z. Y. Qiu, C. M. Zhao, W. C. Wei, W. X. Chen, Z. J. Li, Y. T. Qu, J. C. Dong, J. Luo, Z. Y. Li and Y. Wu, In Situ Thermal Atomization to Convert Supported Nickel Nanoparticles into Surface-Bound Nickel Single-Atom Catalysts, *Angew. Chem., Int. Ed.*, 2018, **57**, 14095.

16 L. W. Xing, Y. J. Jin, Y. X. Weng, R. Feng, Y. J. Ji, H. Y. Gao, X. Chen, X. W. Zhang, D. D. Jia and G. Wang, Top-down synthetic strategies toward single atoms on the rise, *Matter*, 2022, **5**, 788–807.

17 C. Xia, Y. Qiu, Y. Xia, *et al.*, General synthesis of single-atom catalysts with high metal loading using graphene quantum dots, *Nat. Chem.*, 2021, **13**, 887–894.

18 J. C. Hao, Z. C. Zhuang, J. C. Hao, C. Wang, S. L. Lu, F. Duan, F. P. Xu, M. L. Du and H. Zhu, Interatomic Electronegativity Offset Dictates Selectivity When Catalyzing the CO_2 Reduction Reaction, *Adv. Energy Mater.*, 2022, **12**, 2200579.

19 Q. Yang, H. X. Liu, P. Yuan, Y. Jia, L. Z. Zhuang, H. W. Zhang, X. C. Yan, G. H. Liu, Y. F. Zhao, J. Z. Liu, S. Q. Wei, L. Song, Q. L. Wu, B. Q. Ge, L. Z. Zhang, K. Wang, X. Wang, C. R. Chang and X. D. Yao, Single Carbon Vacancy Traps Atomic Platinum for Hydrogen Evolution Catalysis, *J. Am. Chem. Soc.*, 2022, **144**(5), 2171–2178.

20 P. Yu, L. Wang, F. Sun, Y. Xie, X. Liu, J. Ma, X. Wang, C. Tian, J. Li and H. Fu, Co Nanoislands Rooted on Co–N–C Nanosheets as Efficient Oxygen Electrocatalyst for Zn–Air Batteries, *Adv. Mater.*, 2019, **31**, 1901666.

21 J. Z. Li, H. Li, W. F. Xie, S. J. Li, Y. K. Song, K. Fan, J. Y. Lee and M. F. Shao, Flame-Assisted Synthesis of O-Coordinated Single-Atom Catalysts for Efficient Electrocatalytic Oxygen Reduction and Hydrogen Evolution Reaction, *Small Methods*, 2022, **6**, 2101324.

 This journal is © The Royal Society of Chemistry 2024

Published on 31 January 2024. Downloaded on 12/2/2024 2:15:32 PM.

22 Z. Lu, B. Wang, Y. Hu, W. Liu, Y. Zhao, R. Yang, Z. Li, J. Luo, B. Chi, Z. Jiang, M. Li, S. Mu, S. Liao, J. Zhan and X. Sun, An Isolated Zinc–Cobalt Atomic Pair for Highly Active and Durable Oxygen Reduction, *Angew. Chem., Int. Ed.*, 2019, **58**, 2622.

23 H. S. Gong, Z. X. Wei, Z. C. Gong, J. J. Liu, G. L. Ye, M. M. Yan, J. C. Dong, C. Allen, J. B. Liu, K. Huang, R. Liu, G. C. He, S. L. Zha and H. L. Fei, Low-Coordinated Co-N-C on Oxygenated Graphene for Efficient Electrocatalytic H_2O_2 Production, *Adv. Funct. Mater.*, 2022, **32**, 2106886.

24 Z. Q. Deng, C. Q. Ma, Z. R. Li, Y. S. Luo, L. C. Zhang, S. J. Sun, Q. Liu, J. Du, Q. P. Lu, B. Z. Zheng and X. P. Sun, High-Efficiency Electrochemical Nitrate Reduction to Ammonia on a Co_3O_4 Nanoarray Catalyst with Cobalt Vacancies, *ACS Appl. Mater. Interfaces*, 2022, **14**(41), 46595–46602.

25 F. L. Zhao, G. T. Hai, X. Li, Z. Y. Jiang and H. H. Wang, Enhanced electrocatalytic nitrate reduction to ammonia on cobalt oxide nanosheets via multiscale defect modulation, *Chem. Eng. J.*, 2023, **461**, 141960.

26 Z. N. Zhang, Q. L. Hong, X. H. Wang, H. Huang, S. N. Li and Y. Chen, Au Nanowires Decorated Ultrathin Co_3O_4 Nanosheets toward Light-Enhanced Nitrate Electroreduction, *Small*, 2023, **19**, 2300530.

27 L. Mi, Q. Huo, J. Cao, X. Chen, H. Yang, Q. Hu and C. He, Achieving Synchronization of Electrochemical Production of Ammonia from Nitrate and Ammonia Capture by Constructing a "Two-In-One" Flow Cell Electrolyzer, *Adv. Energy Mater.*, 2022, **12**, 2202247.

28 Y. T. Wang, C. B. Liu, B. Zhang and Y. F. Yu, Self-template synthesis of hierarchically structured Co_3O_4@NiO bifunctional electrodes for selective nitrate reduction and tetrahydroisoquinolines semi-dehydrogenation, *Sci. China Mater.*, 2020, **63**(12), 2530–2538.

29 P. Huang, T. Fan, X. Ma, J. Zhang, Y. Zhang, Z. Chen and X. Yi, 3D Flower-Like Zinc Cobaltite for Electrocatalytic Reduction of Nitrate to Ammonia under Ambient Conditions, *ChemSusChem*, 2022, **63**(12), 2530–2538.

30 Z. Y. Wu, M. Karamad and X. Yong, Electrochemical ammonia synthesis via nitrate reduction on Fe single atom catalyst, *Nat. Commun.*, 2021, **12**, 2870.

31 J. Li, M. Li, N. An, S. Zhang, Q. Song, Y. Yang, J. Li and X. Liu, Boosted ammonium production by single cobalt atom catalysts with high Faradic efficiencies, *Proc. Natl. Acad. Sci. U. S. A.*, 2022, **119**, e2123450119.

32 J. Li, Y. Zhan, C. Li, L. Zheng, E. Peti, K. Qi, Y. Zhan, H. Wu, W. Wang, A. Tiberj, X. Wang, M. Chhowalla, L. Lajaunie, R. Yu and D. Voiry, 3.4% Solar-to-Ammonia Efficiency from Nitrate Using Fe Single Atomic Catalyst Supported on MoS_2 Nanosheets, *Adv. Funct. Mater.*, 2022, **32**, 2108316.

33 X. Zhao, X. Jia, Y. He, H. Zhang, X. Zhou, H. Zhang, S. Zhang, Y. Dong, X. Hu, A. V. Kuklin, G. V. Baryshnikov, H. Ågren and G. Hu, Two-dimensional BCN matrix inlaid with single-atom-Cu driven electrochemical nitrate reduction reaction to achieve sustainable industrial-grade production of ammonia, *Appl. Mater. Today*, 2021, **25**, 101206.

34 Y. Wang, H. Yin, F. Dong, X. Zhao, Y. Qu, L. Wang, Y. Peng, D. Wang, W. Fang and J. Li, N-Coordinated Cu-Ni Dual-Single-Atom Catalyst for Highly Selective Electrocatalytic Reduction of Nitrate to Ammonia, *Small*, 2023, **19**, 2207695.

35 P. Li, R. Li, Y. Liu, M. Xie, Z. Jin and G. Yu, Pulsed Nitrate-to-Ammonia Electroreduction Facilitated by Tandem Catalysis of Nitrite Intermediates, *J. Am. Chem. Soc.*, 2023, **145**, 6471.

36 Z. Gao, Y. Lai, Y. Tao, L. Xiao, L. Zhang and F. Luo, Constructing Well-Defined and Robust Th-MOF-Supported Single Site Copper for Production and Storage of Ammonia from Electroreduction of Nitrate, *ACS Cent. Sci.*, 2021, **7**, 1066.

37 W. D. Zhang, H. L. Dong and L. Zhou, Fe single-atom catalysts with pre-organized coordination structure for efficient electrochemical nitrate reduction to ammonia, *Appl. Catal., B*, 2022, **317**, 121750.

38 M. R. McCoustra, Water at interfaces, *Phys. Chem. Chem. Phys.*, 2008, **10**, 4676–4677.

39 Y. R. Zhao, X. X. Chang, A. S. Malkani, X. Yang, L. Thompson, F. Jiao and B. J. Xu, Speciation of Cu Surfaces During the Electrochemical CO Reduction Reaction, *J. Am. Chem. Soc.*, 2020, **142**(21), 9735–9743.

40 W. He, J. Zhang, S. Dieckhöfer, S. Varhade, A. C. Brix, A. Lielpetere, S. Seisel and R. C. João, Junqueira and W. Schuhmann, Splicing the active phases of copper/cobalt-based catalysts achieves high-rate tandem electroreduction of nitrate to ammonia, *Nat. Commun.*, 2022, **13**, 1129.